Scripta Materialia 255 (2025) 116396

Contents lists available at ScienceDirect

Scripta Materialia

journal homepage: www.journals.elsevier.com/scripta-materialia

Intermittent *in-situ* high-resolution X-ray microscopy of 400-nm porous glass under uniaxial compression: Study of pore changes and crack formation

Sebastian Schäfer [a], François Willot [b], Hrishikesh Bale [c], Mansoureh Norouzi Rad [c], Stephen T. Kelly [c], Dirk Enke [d], Juliana Martins de Souza e Silva [a,e,*]

[a] *Institute of Physics, Martin-Luther-Universität Halle-Wittenberg, Heinrich-Damerow-Str. 4, Halle (Saale) 06120, Germany*
[b] *Mines ParisTech, Centre for Mathematical Morphology, PSL - Research University, 35 rue St-Honoré, Fontainebleau 77300, France*
[c] *Carl Zeiss X-ray Microscopy, Hopyard Road # 100, Pleasanton, CA 94588, USA*
[d] *Institute of Chemical Technology, Universität Leipzig, Linnéstr. 3, Leipzig 04103, Germany*
[e] *Fraunhofer Institute for Microstructure of Materials and Systems IMWS, Walter-Hülse Str. 1, Halle (Saale) 06120, Germany*

ARTICLE INFO

Keywords:
X-ray computed tomography
Compression test
Controlled pore glass
Phase-field method
Crack propagation

ABSTRACT

Understanding the relationship between the structure of porous glasses and their failure behavior is crucial for developing reliable porous glasses for specific applications. In this study, we used nanometer resolution X-ray computed tomography (nano-CT) to image a controlled pore glass (CPG) with 400 nm-sized pores under *in-situ* uniaxial compression. Our results demonstrate that *in-situ* nano-CT is an excellent tool for identifying damage mechanisms in 400 nm pore glass. It allowed us to track changes in the shape of pores and pore walls during compression until the specimen failed. We also used computational tools to analyze the microstructural changes within the CPG sample, mapping displacements and strain fields. Additionally, we simulated the behavior of the CPG using a Fast Fourier Transform/Phase Field method. Both experimental and numerical data revealed local shear deformation occurring along bands, consistent with the appearance and propagation of ± 45-degree cracks.

Porous silica monoliths can be synthesized by phase separation processes, either through the thermally-induced phase separation in alkali borosilicate glasses or the polymer-induced phase separation in sol-gel processes [1–3]. They are used in optics, heterogeneous catalysis, sensors, chromatography, and as hosts for nanoparticles and bio-compounds mainly due to their high specific surface area and high thermal and chemical resistances [1,3]. The fine-tuning of the synthetic parameters allows tailoring the silica pore network, resulting in monomodal or hierarchical pore structures with pore size distribution ranging from nano- to micrometer scales [1,3].

For use in any of those contexts, the mechanical stability of porous silica is an essential requirement to guarantee resilience, load-bearing capacity, and fatigue resistance [4]. However, regardless of their potential, porous silica monoliths' poor mechanical stability hinders their widespread use at an industrial scale. Questions remain open concerning the predictability of their mechanical properties, particularly the onset of local damage and its propagation throughout the volume until collapse. *In-situ* three-dimensional (3D) X-ray imaging has already been used in materials science for following structural evolution over time, whether during manufacturing, throughout service, or in understanding the events leading to failure [5]. It enables the detection of large [6] to sub-micrometric pores [7], and was used to image mechanical tests in laboratories and synchrotron facilities during *ex-situ* and *in-situ* indentation and compression [8–10]. When combined with Digital Volume Correlation (DVC) analysis, *in-situ* X-ray CT imaging data can produce 3D strain maps of the samples. To do this, a three-dimensional grid defined in the reference (undeformed) volume allows the displacement to be calculated for each point of the grid throughout the deformation process [11]. This displacement information is essential for analyzing the mechanical behavior, as the DVC analysis can quantitatively characterize the changes in the internal structure and deformation of the porous glass. Experimentally estimated local variations in the microstructure, displacement fields, and strain fields allow a quantitative study of the internal deformation and damage process of materials [12],

* Corresponding author at: Fraunhofer Institute for Microstructure of Materials and Systems IMWS, Walter-Hülse Str. 1, Halle (Saale) 06120, Germany.
E-mail address: juliana.martins@physik.uni-halle.de (J.M. de Souza e Silva).

https://doi.org/10.1016/j.scriptamat.2024.116396
Received 24 April 2024; Received in revised form 19 September 2024; Accepted 21 September 2024
Available online 26 September 2024

can help to establish potential routes to explain failure mechanisms [8] by providing valuable insights into the mechanical properties and behavior of porous materials under load. Indeed, the DVC method allows to solve the problems of microstructural deformation and crack initiation and propagation in materials [12–14].

The observation of spatial and temporal damage occurrences is critical for the understanding of a material's behavior [15]. Here we investigated a porous glass sample of ~50 μm-diameter with interconnected 400 nm-sized pores (Fig. A1) under *in-situ* uniaxial compression with high-resolution X-ray imaging. We conducted full 3D scans of the CPG400 sample in five steps: step 0 is the initial state, while steps 1 to 4 involve vertical (z-axis) compression. Step 4 resulted in complete sample failure. The stress-strain curve shows sudden pressure changes (arrows in Figs. 1a, A2) typical in interrupted *in-situ* tomography due to load relaxation rather than sample deformation (increments of 50–60 mN). The force needed for failure is about ten times less than that for non-porous glass (Fig. A3). In the dataset, brighter voxels represent glass regions and darker voxels indicate pores (Fig. A4). The volumetric images after each compression (Fig. 1b–f) show shape changes and damage evolution, with noticeable dislocations after the second and third compressions (Fig. 1d, and e) and a large crack after the fourth (Fig. 1f).

Comparing virtual slices (Fig. 2a–e) before and after the compressions reveals smaller-scale changes at the edges and center (Fig. 2f–j), with vertical movements and slight densification in the top layer (Fig. 2, dotted lines). Cracking appears at ±45° angles after the third compression (red arrows in Fig. 2d, i) and widen after the fourth (Fig. 2e). In the center slice, this crack disappears after the fourth compression (Fig. 2j), likely due to chipping.

A small segmented volume displays pores in 3D (Fig. 3a–e) and the large crack from the fourth compression (Fig. 3e). Detailed views illustrate pore and wall shape changes with each compression. Specifically, a pore wall merges with another above it (Fig. 3a–c), buckles after the third compression (Fig. 3d), and breaks after the fourth (Fig. 3e). Another pore closes after three compressions (Fig. 3a-d) and reopens after the fourth (Fig. 3e). A pair of pores merges after the third compression (Fig. 3d), while a pore wall collapses after the first compression, closing the pore in the final compression.

We used DVC (global approach) to analyze the strain resulting from axial compression applied to the CPG400 material. Our results show a heterogeneous strain field within the CPG400 specimen (Fig. 3f–i).

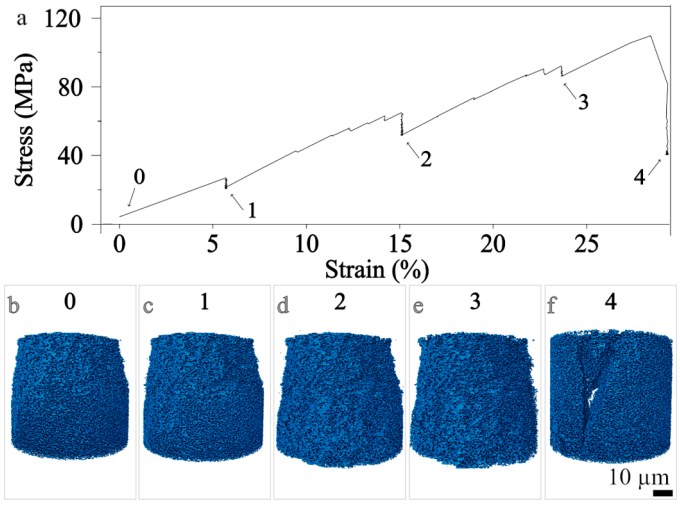

Fig. 1. *In-situ* nano-CT characterization of CPG400 sample. (a) Stress-strain curve for incremental compression. Pauses for CT scans were taken at the load drops marked in the graph, (b–f) CPG400 volumetric reconstructions for uncompressed sample (0) and after incremental compressions (successively 1 to 4).

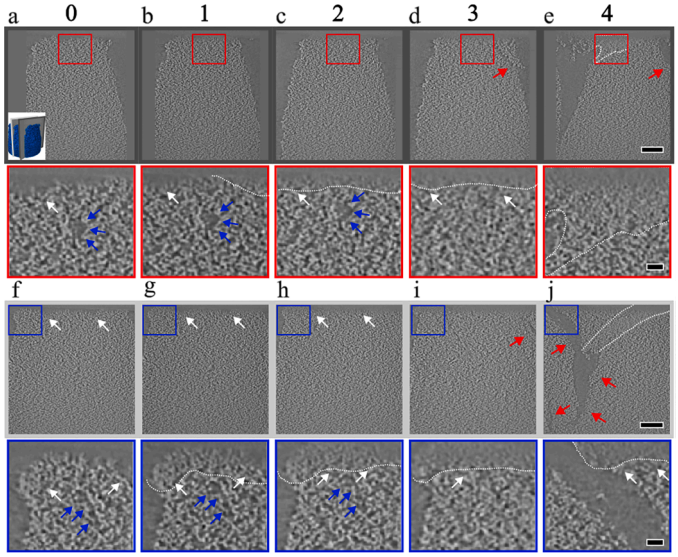

Fig. 2. CPG400 vertical virtual slices (a–e) near the edge and (f–j) in the center of the specimen, for uncompressed specimen (0) and after four incremental compressions (1–4). The volumetric image in the detail in the lower left corner of (a) shows the position of the virtual slices in the conical sample (edge a–e; center f–j). Areas within the red and blue squares are magnified immediately below. White dotted lines indicate regions of sample densification, red arrows indicate areas of cracking and sample detachment, blue arrow indicates the same point of the sample moving up due to compression. Scale bars: 20 μm and 2 μm (red and blue squares).

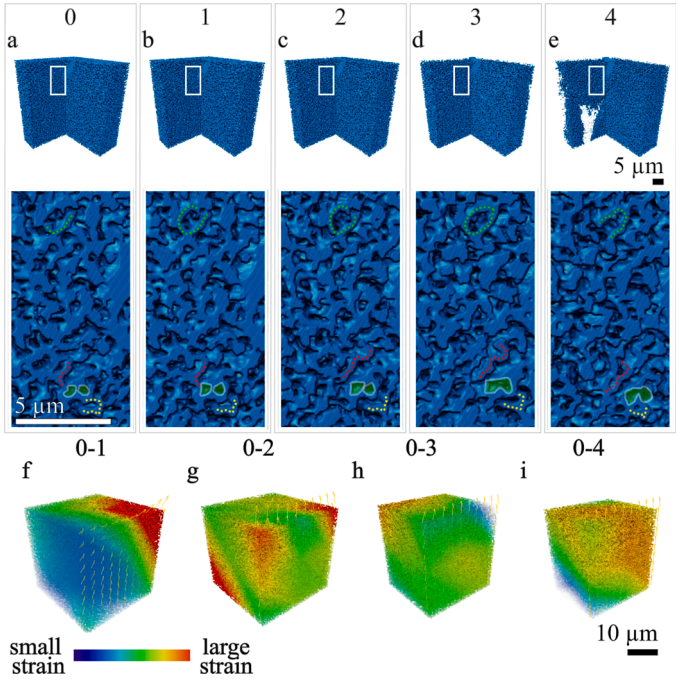

Fig. 3. Volumetric rendering of a small volume of interest of the CPG400 specimen. (a) uncompressed and (b-e) after successive first to fourth compressions. The area highlighted within the white boxes is shown immediately below. Dotted lines follow the shape and position change of pore walls and light green patches highlight two pores that merge. (f-i) Strain component in the axial direction (Ezz) of the CPG400 vol shown above (250×250×300), with data computed between each compressed state (1–4) and the uncompressed state (0), with the displacement vectors (calculated between each compressive state).

Specifically, higher strain is aligned at angles of ±45° relative to the direction of loading, with the highest strain values seen after the third compression stage (Fig. 3h, in orange/red). Notably, this stage coincided with the appearance of the first crack (Fig. 2d and i). Conversely, the lowest strain values were observed after the fourth compression (Fig. 3i), which ultimately led to the specimen's collapse.

In the phase-field predictions of failure, the value for the fracture toughness g_c was first identified so that a macroscopic crack occurs at a strain of about 30 %. The macroscopic stress-strain response for one specimen considered in our analysis using the values $g_c=g_c^0$, $g_c=1.2g_c^0$ and $g_c=1.4g_c^0$, with g_c^0 =1000 J/m^2 (Fig. 4a, solid lines) shows the intermediate value being consistent with a fracture at about 30 %. Mode-I critical energy release rates reported in the literature for silica-based glasses are in the range of 10 to 20 J/m^2 [16,17] and significantly larger, up to several hundreds, for mode-II [18]. Several factors contribute to the comparatively high value used in the present model. First, porosity, up to 60 % in our case, generally decreases the fracture toughness that can be measured experimentally in brittle materials [19, 20]. Second, the fracture toughness has been identified in the present work with a macroscopic failure strain of 30 % whereas larger samples exhibit lower strain at failure. A systematic study, left to future work, would be needed to address the influence of the sample size and microstructure variability on the choice of the parameter g_c. The maximum of the phase-field reaches its highest value, very close to one for a deformation of about 15 % (dashed lines). The mean of the phase field is also represented (Fig. 4a, black curve) for the highest fracture toughness, which shows that the density of crack surfaces strongly increases at about 30 %. For one specific slice (Fig. 4b), FFT maps equivalent strain and phase-field (Fig. 4c and d, respectively) obtained for the final loading step show that the cracks are oriented at angles of ±45° with respect to the loading direction. A comparison of the 3D representation of the numerically predicted crack (Fig. 4e) after near-complete failure and the experimentally obtained crack (Fig. 4f and g, respectively, for the entire specimen and a smaller volume selected within it) shows that, although the crack is not located in the exact same region as the actual final visible experimental crack, it has a similar orientation. The location of the crack in the FFT calculations and in the experiment differ by about 0.7 μm. Further analysis of the FFT data shows that at the onset of crack initiation, the phase field is localized in several regions of the microstructure. These regions rapidly coalesce into one main crack (Fig. 5).

The design of longer-lasting porous materials requires studying material failure and identifying damage mechanisms. In general, damage originates at the nanoscale, accumulates, and grows until microscopic and macroscopic defects are formed [15]. Stress-strain curves describe the structural changes averaged statistically over the entire measured specimen and, thus, assume homogeneity in stress–strain relationships throughout the sample, neglecting the complex modification of internal microstructural morphologies (e.g., porosity) due to local changes [21]. Here, the *in-situ* mechanical testing of a ~50 μm-diameter CPG400 specimen under incremental loading in a nano-CT shows that a force of 150 mN caused the first crack to appear in the specimen analyzed, and further compression up to 200 mN caused the specimen to collapse (Fig. A2). In addition to force-displacement and stress-strain curves, *in-situ* nano-CT allows the observation of damage mechanisms at high resolution. Microscopically, it allowed visualization of individual pores, the interconnected wall network, and their local interactions and spatial arrangement along successive compression states (Figs. 2 and 3). Under uniaxial vertical strain, changes in the pore volume and the porosity are functions of the changes in vertical overburden stress [22]. As the load increased, the pores of CPG400 coalesced and increased in volume (as shown in Fig 3i), but also decreased in size, causing densification of the specimen (Fig. A5). This densification phenomenon was more apparent in the upper region of the sample, potentially due to the roughness of the top surface of the sample, thus contributing to the non-linear strain stage [23]. In addition, nano-CT allowed the visualization of densification bands in the vicinity of the larger cracks. This phenomenon suggests a progressive failure mechanism, where the initial crack serves as a precursor for the development of more extensive damage in the material under continued compression. The simulation data corroborate that following the crack's initiation, the phase fields swiftly coalesce to form one primary crack (Fig. 5).

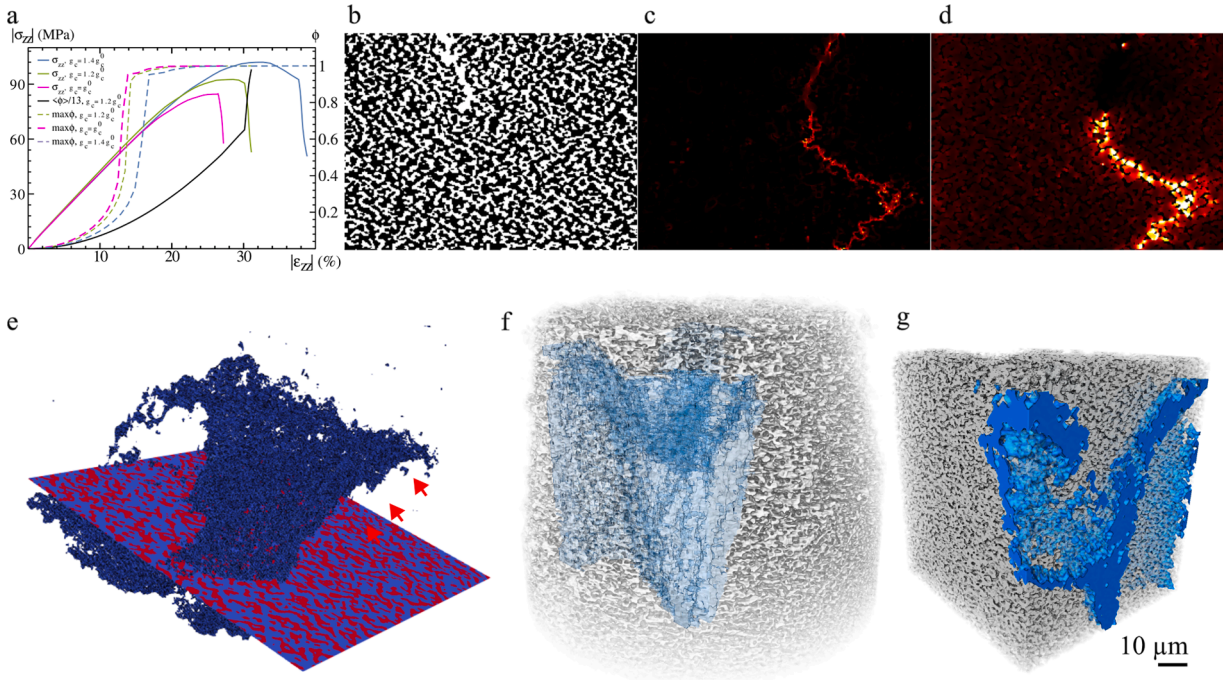

Fig. 4. Phase-field predictions of failure. (a) Simulated strain-stress curve for two specimens of the same sample, (b) binarized slice xy=184, (c) FFT predictions of the von Mises equivalent strain (highest values in yellow, lowest in black) along a 2D-cut of slice xy=184 and (d) corresponding phase-field φ (φ=1: yellow, damaged material; φ=0: dark, sane material). Three-dimensional view of the crack formed after (e) phase-field simulation, and experimental compression crack in blue superimposed on the (f) volumetric image and (g) on a smaller work volume of the uncompressed specimen.

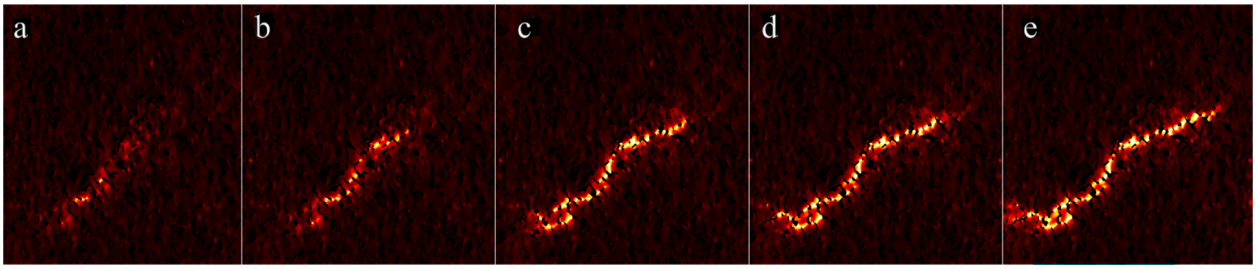

Fig. 5. Phase-field images (2D cut) during compression loading. The overall strain in the loading direction increases from (a) 0.1 to (e) 28 %.

The high-resolution and image quality of nano-CT provides sufficient feature contrast to allow the use of DVC to estimate 3D displacements, which were then translated into strain fields. The analysis of strain maps revealed heterogeneous changes occurring within the specimen, indicating the presence of a heterogeneous strain field in the CPG400 material. This heterogeneity can be attributed to the microstructural nature of the material, as previously suggested [11]. As observed by others [11], the local strain heterogeneities decreased with increasing load (Fig. 3g–i). This suggests that regions initially subjected to high deformation at the onset of loading experience a relocalization of the imposed strain, resulting in reduced deformation in those areas. As supported by others [11], these results highlight the critical role of local strain heterogeneities in shaping the overall mechanical behavior of materials, and illustrates the dynamic behavior of the CPG400 and its response to applied loads.

The virtual nano-CT slices allow to visualize the densification of the sample at the top of the specimen after each compression state and the formation of densification regions formed as bands (Fig. 2). Due to the resolution limit of the images obtained, the segmentation protocol used does not detect the smaller pores within the densification bands (Fig. A6), thus, the densification calculations (Fig. A5) also miss this information. As in [24], the threshold used for segmentation was chosen so that the volume fraction of the 3D image had a porosity as close as possible to the known porosity of the sample measured by the standard method (Fig. A1). This choice seems adequate for the DVC analysis and phase-field simulations performed, since it allowed the detection of the pores, their interconnection, and local variations in the CPG400 microstructure.

The combined Fourier/phase-field method seems to be suitable for the numerical simulation of the behavior of the CPG400 subjected to uniaxial compression. The results obtained indicate the presence of a local shear deformation along bands, possibly oriented at $\pm 45^{\circ}$, as observed experimentally. This mode of deformation, with varying angles, has been observed in other materials such as metallic glasses [25].

The study of material failure and the identification of damage mechanisms are critical to the design of longer-lasting porous materials. Repeated experiments would be necessary to obtain statistically relevant data to confirm the forces required to cause damage to the CPG400. In addition, for brittle materials, it is well known that specimen size affects the measured mechanical properties, and the underlying mechanics at different length scales that govern brittle material behavior are not yet fully understood [26,27]. This paper does not address the size issue and is concerned only with local structural changes in the CPG400.

In summary, here we investigated the local deformation of 400 nm-sized controlled pore glass under mechanical stress events using *in-situ* uniaxial compression with high-resolution X-ray computed tomography, Digital Volume Correlation, and FFT numerical modelling. Our results show that the high-resolution 3D images effectively capture the structural deformation that occurs as a result of the vertical compression of the specimen. They illustrate pore densification, crack initiation, propagation, and failure of the sub-micrometric porous silica studied. Analysis of different areas of the specimen revealed the internal deformation that occurs during compression, including the dynamic changes of specific pores and walls in three-dimensions. The images enable to detect areas of densification, although higher-resolution imaging may be required to accurately quantify the densification at the top of the specimen or in bands within it. The experimental results suggest that the crack propagation mechanisms were controlled by pre-existing cracks that formed at a similar angle.

Without any a priori knowledge of the location of the crack initiation, the combined Fourier/phase-field method appears suitable for the numerical simulation of the CPG400 and shows that the cracks formed due to compression are oriented at angles of $\pm 45^{\circ}$ to the loading direction. The results obtained indicate the presence of local shear deformation along bands, possibly oriented at $\pm 45^{\circ}$ degrees, as also observed experimentally. Repeated experiments would be required to obtain statistically relevant data on the stress-strain relationship in this specimen, although it remains unclear whether the small-scale experimental and numerical results accurately capture the damage propagation mechanisms in large specimens.

Funding

This research did not receive any specific grant from funding agencies in the public, commercial, or not-for-profit sectors.

Statement

During the preparation of this work the author(s) used FhGenie and DeepLWrite to improve readability of a few passages of the text. After using this tool/service, the author(s) reviewed and edited the content as needed and take(s) full responsibility for the content of the publication.

CRediT authorship contribution statement

Sebastian Schäfer: Writing – review & editing, Writing – original draft, Investigation, Formal analysis. **François Willot:** Writing – review & editing, Writing – original draft, Visualization, Methodology, Formal analysis, Conceptualization, Investigation. **Hrishikesh Bale:** Writing – review & editing, Validation. **Mansoureh Norouzi Rad:** Methodology, Investigation. **Stephen T. Kelly:** Writing – review & editing, Resources, Methodology. **Dirk Enke:** Writing – review & editing, Writing – original draft, Validation, Resources, Conceptualization. **Juliana Martins de Souza e Silva:** Writing – review & editing, Writing – original draft, Resources, Project administration, Investigation, Formal analysis, Conceptualization.

Declaration of competing interest

The authors declare that they have no known competing financial interests or personal relationships that could have appeared to influence the work reported in this paper.

Acknowledgment

We are grateful to an anonymous reviewer for useful comments that

helped to improve the manuscript.

Supplementary materials

Supplementary material associated with this article can be found, in the online version, at doi:10.1016/j.scriptamat.2024.116396.

References

[1] A. Feinle, M.S. Elsaesser, N. Husing, Sol-gel synthesis of monolithic materials with hierarchical porosity, Chem. Soc. Rev. 45 (12) (2016) 3377–3399.
[2] A. Inayat, B. Reinhardt, J. Herwig, C. Kuster, H. Uhlig, S. Krenkel, E. Raedlein, D. Enke, Recent advances in the synthesis of hierarchically porous silica materials on the basis of porous glasses, New J. Chem. 40 (5) (2016) 4095–4114.
[3] A. Inayat, B. Reinhardt, H. Uhlig, W.D. Einicke, D. Enke, Silica monoliths with hierarchical porosity obtained from porous glasses, Chem. Soc. Rev. 42 (9) (2013) 3753–3764.
[4] D. Enke, R. Glaser, U. Tallarek, Sol-gel and porous glass-based silica monoliths with hierarchical pore structure for solid-liquid catalysis, Chem. Ing. Tech. 88 (11) (2016) 1561–1585.
[5] E. Maire, P.J. Withers, Quantitative X-ray tomography, Int. Mater. Rev. 59 (1) (2014) 1–43.
[6] B. Wang, L.J. Sun, B. Pan, Mapping internal deformation fields in 3D printed porous structure with digital volume correlation, Polym. Test. 78 (2019) 105945.
[7] F.V. Luna, A.K. Maurya, J.M. de Souza e Silva, G. Dittrich, T. Paul, D. Enke, P. Huber, R. Wehrspohn, M. Steinhart, Straight versus spongy: effect of tortuosity on polymer imbibition into nanoporous matrices assessed by segmentation-free analysis of 3D sample reconstructions, J. Phys. Chem. C 126 (30) (2022) 12765–12779.
[8] A. Buljac, C. Jailin, A. Mendoza, J. Neggers, T. Taillandier-Thomas, A. Bouterf, B. Smaniotto, F. Hild, S. Roux, Digital volume correlation: review of progress and challenges, Exp. Mech. 58 (5) (2018) 661–708.
[9] T.T. Nguyen, J. Yvonnet, M. Bornert, C. Chateau, Initiation and propagation of complex 3D networks of cracks in heterogeneous quasi-brittle materials: direct comparison between in situ testing-microCT experiments and phase field simulations, J. Mech. Phys. Solids. 95 (2016) 320–350.
[10] M. Mostafavi, R. Bradley, D.E.J. Armstrong, T.J. Marrow, Quantifying yield behaviour in metals by X-ray nanotomography, Sci. Rep. 6 (2016) 34346. -Uk.
[11] H. Tran, P. Doumalin, C. Delisee, J.C. Dupre, J. Malvestio, A. Germaneau, 3D mechanical analysis of low-density wood-based fiberboards by X-ray microcomputed tomography and digital volume correlation, J. Mater. Sci. 48 (8) (2013) 3198–3212.
[12] F. Xu, Quantitative characterization of deformation and damage process by digital volume correlation: a review, Theor. Appl. Mech. Lett. 8 (2) (2018) 83–96.
[13] S.R. Daemi, X. Lu, D. Sykes, J. Behnsen, C. Tan, A. Palacios-Padros, J. Cookson, E. Petrucco, P.J. Withers, D.J.L. Brett, P.R. Shearing, 4D visualisation of in situ nano-compression of Li-ion cathode materials to mimic early stage calendering, Mater. Horiz. 6 (3) (2019) 612–617.
[14] D. Sykes, R. Hartwell, R.S. Bradley, T.L. Burnett, B. Hornberger, R.J. Garwood, P. J. Withers, Time-lapse three-dimensional imaging of crack propagation in beetle check for cuticle, Acta Biomater. 86 (2019) 109–116.
[15] B.M. Patterson, N.L. Cordes, K. Henderson, J.C.E. Mertens, A.J. Clarke, B. Hornberger, A. Merkle, S. Etchin, A. Tkachuk, M. Leibowitz, D. Trapp, W. Qiu, B. Zhang, H. Bale, X. Lu, R. Hartwell, P.J. Withers, R.S. Bradley, *In situ* laboratory-based transmission x-ray microscopy and tomography of material deformation at the nanoscale, Exp. Mech. 56 (9) (2016) 1585–1597.
[16] O. Rodriguez, A. Matinmanesh, S. Phull, E.H. Schemitsch, P. Zalzal, O.M. Clarkin, M. Papini, M.R. Towler, Silica-based and borate-based, titania-containing bioactive coatings characterization: critical strain energy release rate, residual stresses, hardness, and thermal expansion, J. Funct. Biomater. 7 (4) (2016).
[17] T. Du, M. Blum, C. Chen, M.G. Muraleedharan, A.C.T. van Duin, P. Newell, Nanomechanical investigation of the interplay between pore morphology and crack orientation of amorphous silica, Eng. Fract. Mech. 250 (2021).
[18] S.R. Choi, R.W. Kowalik, Interlaminar crack growth resistances of various ceramic matrix composites in mode I and mode II loading, J. Eng. Gas Turb. Power 130 (3) (2008).
[19] J. Uhl, A. Doitrand, S. Meille, Variability in porous ceramic fracture: influence of apparent density and critical pores, J. Eur. Ceram. Soc. 43 (7) (2023) 2875–2883.
[20] X. Xiong, Q.L. Zeng, Y.H. Wang, Y. Li, Pinning cracks by microstructure design in brittle materials, J. Mech. Phys. Solids 183 (2024).
[21] S. Peth, J. Nellesen, G. Fischer, R. Horn, Non-invasive 3D analysis of local soil deformation under mechanical and hydraulic stresses by mu CT and digital image correlation, Soil Till Res. 111 (1) (2010) 3–18.
[22] R.W. Zimmerman, Pore volume and porosity changes under uniaxial strain conditions, Transp. Porous Media 119 (2) (2017) 481–498.
[23] J.F. Zhang, Y.F. Shen, Y.X. Sun, J.X. Yang, Y. Gong, K. Wang, Z.Q. Zhang, X. H. Chen, L. Bai, Design and mechanical testing of porous lattice structure with independent adjustment of pore size and porosity for bone implant, J. Mater. Res. Technol. 18 (2022) 3240–3255.
[24] A. Rouwane, P. Doumalin, R. Bouclier, J.C. Passieux, J.N. Perie, Architecture-driven digital volume correlation: application to the analysis of *in-situ* crushing of a polyurethane foam, Exp. Mech. 63 (5) (2023) 897–913.
[25] Z.F. Zhang, J. Eckert, L. Schultz, Fatigue and fracture behavior of bulk metallic glass, Metall. Mater. Trans. A 35 (11) (2004) 3489–3498.
[26] M. Molavian Jazi, M. Ghayour, S. Ziaei-Rad, E. Maani Miandoab, Effect of size on the dynamic behaviors of atomic force microscopes, Microsyst. Technol. 24 (4) (2018) 1755–1765.
[27] W.N. Sharpe, Murray lecture - Tensile testing at the micrometer scale: opportunities in experimental mechanics, Exp. Mech. 43 (3) (2003) 228–237.